

Stress-induced phase transitions in nanoscale  $\text{CuInP}_2\text{S}_6$ Anna N. Morozovska<sup>1,\*</sup>, Eugene A. Eliseev<sup>2</sup>, Sergei V. Kalinin<sup>3,†</sup>, Yulian M. Vysochanskii<sup>4</sup>, and Petro Maksymovych<sup>3,‡</sup><sup>1</sup>*Institute of Physics, National Academy of Sciences of Ukraine, 46, pr. Nauky, 03028 Kyiv, Ukraine*<sup>2</sup>*Institute for Problems of Materials Science, National Academy of Sciences of Ukraine, Krjijanovskogo 3, 03142 Kyiv, Ukraine*<sup>3</sup>*Center for Nanophase Materials Sciences, Oak Ridge National Laboratory, Oak Ridge, Tennessee 37831, USA*<sup>4</sup>*Institute of Solid State Physics and Chemistry, Uzhhorod University, 88000 Uzhhorod, Ukraine*

(Received 31 March 2021; revised 10 July 2021; accepted 19 July 2021; published 2 August 2021)

Using the Landau-Devonshire approach and available experimental results, we constructed multiwell thermodynamic potential of the layered ferroelectric  $\text{CuInP}_2\text{S}_6$  (CIPS). The analysis of temperature dependences of the dielectric permittivity and lattice constants for different applied pressures unexpectedly reveals the critically important role of a nonlinear electrostriction in this material. With the nonlinear electrostriction included we calculated the temperature and pressure phase diagrams and spontaneous polarization of a bulk CIPS, within the assumed range of applicable temperatures and applied pressures. Using the developed thermodynamic potential, we revealed the strain-induced phase transitions in thin epitaxial CIPS films, as well as the stress-induced phase transitions in CIPS nanoparticles, the shape of which varies from prolate needles to oblate disks. We also revealed the strong influence of a mismatch strain, elastic stress, and shape anisotropy on the phase diagrams and polar properties of a nanoscale CIPS, and derived analytical expressions allowing for elastic control of the nanoscale CIPS polar properties. Hence obtained results can be of particular interest for the strain engineering of nanoscale layered ferroelectrics.

DOI: [10.1103/PhysRevB.104.054102](https://doi.org/10.1103/PhysRevB.104.054102)

## I. INTRODUCTION

Multiferroics [1–3], such as solid-state ferroics with coupled magnetoelectric and/or magnetoelastic orderings of different type, are among the most fascinating objects of fundamental research [4–6] and reveal very promising application perspectives for advanced memories, micro- and nanoelectronics [7], and straintronics [8]. Nanoscale ferroics and multiferroics [9], including ferromagnets, ferroelectrics, and ferroelastics, are the main objects of fundamental research of unusual polar, magnetic, elastic, and structural properties [10,11]. The leading role is played by the emergence of long-range order parameters, such as switchable and often curled electric polarization [12–14] and magnetization [15], and their interaction with elastic subsystem of a nanoscale ferroic. The role of the surface stress, mismatch strains, and surface screening increases significantly with a decrease in the size of nanoscale ferroics [16], very often leading to the unusual morphology of polar domains [17] and three-dimensional vortices [18,19].

Cu-based layered chalcogenides, with a chemical formula  $\text{CuInP}_2\text{Q}_6$  ( $\text{Q}$  is S or Se) [20,21], are promising layered uniaxial ferroelectrics [22–24], with a possibility of downscaling to the limit of a single layer [21,25]. Here S- and Se-based Cu-In compounds have similar structure of individual layers, with  $\text{Cu}^+$  and  $\text{In}^{3+}$  ions counterdisplaced within individual layers,

against the backbone of  $\text{P}_2\text{Q}_6$  anions [26–28]. The spontaneous polarization of the uniaxial ferroelectric  $\text{CuInP}_2\text{S}_6$  ranges from 0.05 to 0.12 C/m<sup>2</sup> [29], and is about 0.025 C/m<sup>2</sup> for the uniaxial ferroelectric  $\text{CuInP}_2\text{Se}_6$  [30]. The ferroelectric (or ferroelectric) phase transition temperature is  $\sim 305$  K for  $\text{CuInP}_2\text{S}_6$  and  $\sim 230$  K for  $\text{CuInP}_2\text{Se}_6$ .

The  $\text{CuInP}_2(\text{S}, \text{Se})_6$  family reveals very unusual features of a nonlinear dielectric response indicating that a spontaneous polarization may exist above the transition temperature [31], extremely large elastic nonlinearity in the direction perpendicular to the layers [32,33], a giant negative electrostriction and dielectric tunability [34], the electrostriction-induced piezoelectricity above the ferroelectric transition temperature [35], morphotropic phase transitions between its monoclinic and trigonal phases [36], and anomalous “bright” domain walls with enhanced local piezoelectric response [37,38].

Despite the significant fundamental and practical interest in  $\text{CuInP}_2\text{Q}_6$ , the polar properties of this material and their analytical dependence on elastic stresses and/or strains are generally unknown. Most notably, the appropriate free-energy functional that can effectively capture the various properties of this material has not been developed. Using the Landau-Devonshire (LD) theoretical approach and available experimental results, here we reconstruct the thermodynamic potential of a layered ferroelectric  $\text{CuInP}_2\text{S}_6$  (CIPS), then calculate the phase diagrams and spontaneous polarization of a bulk CIPS in dependence on temperature and pressure. Using the coefficients of the reconstructed thermodynamic potential, we study the strain-induced phase transitions in CIPS thin films, as well as the stress-induced phase transitions in CIPS ellipsoidal nanoparticles,

\*anna.n.morozovska@gmail.com

†sergei2@ornl.gov

‡maksymovychp@ornl.gov

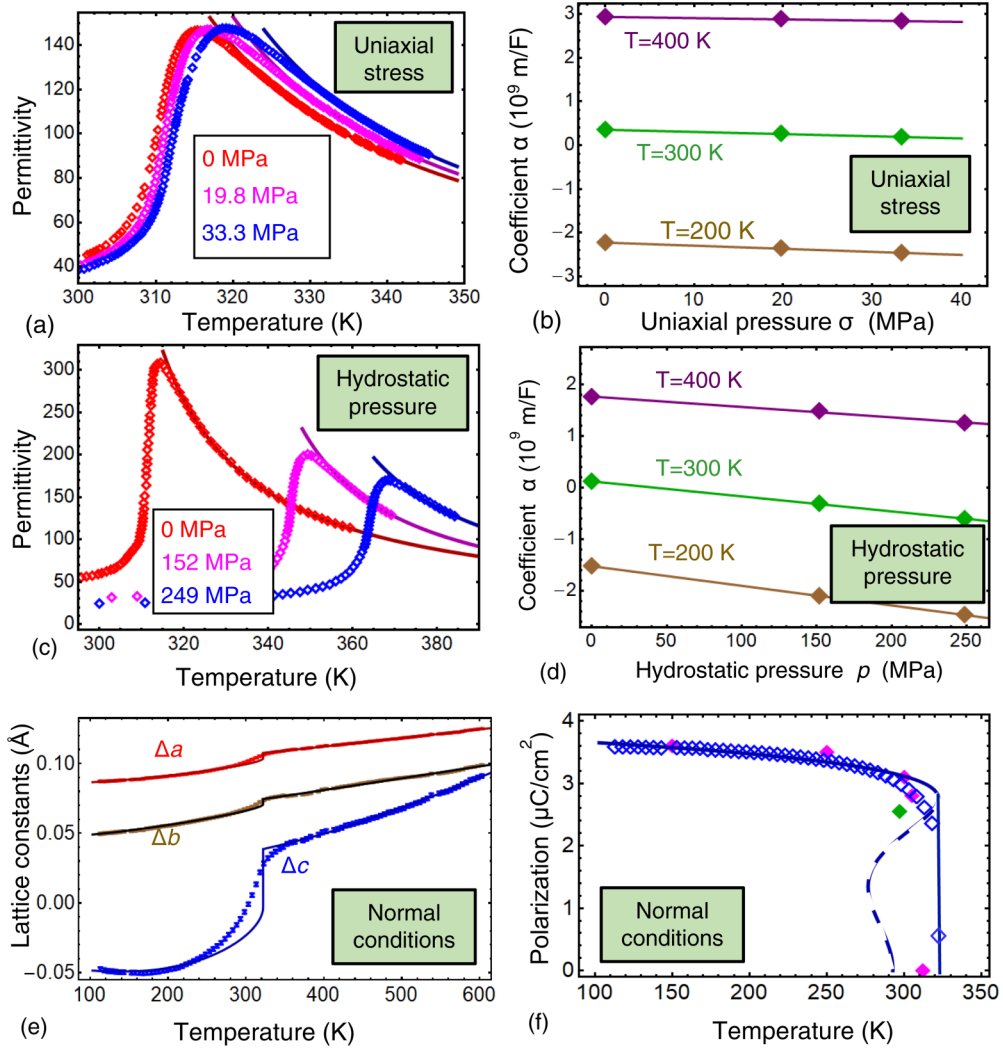


FIG. 1. The temperature dependence of relative dielectric permittivity (a), (c). The dependence of renormalized coefficient  $\alpha$  (b), (d) on the uniaxial (a), (b) and hydrostatic (d) pressure. The temperature dependences of the lattice constants variations  $\Delta a$ ,  $\Delta b$ ,  $\Delta c$  (e); and spontaneous polarization (f) at normal conditions. Symbols are experimental data from Refs. [43–45] for the plots (a)–(d), from Ref. [24] for the plot (e) and from Ref. [46] for the plot (f); solid curves are our fitting.

the shape of which varies from prolate needles to oblate disks.

## II. THEORETICAL DESCRIPTION

### A. Reconstruction of CIPS thermodynamic potential from experiments

Since CIPS is a uniaxial ferroelectric with the one-component ferroelectric polarization component  $P_3$ , the bulk density of the Landau-Ginsburg-Devonshire (LGD) functional is

$$g_{\text{LGD}} = \left( \frac{\alpha}{2} - \sigma_i Q_{i3} \right) P_3^2 + \left( \frac{\beta}{4} - \sigma_i Z_{i33} \right) P_3^4 + \frac{\gamma}{6} P_3^6 + \frac{\delta}{8} P_3^8 - P_3 E_3 + g_{33ij} \frac{\partial P_3}{\partial x_i} \frac{\partial P_3}{\partial x_j}. \quad (1)$$

As is conventional, we assume that only the coefficient  $\alpha$  depends linearly on the temperature  $T$  as  $\alpha(T) = \alpha_T(T - T_C)$ , where  $T_C$  is the Curie temperature of bulk

material. In accordance with classical Landau theory, the coefficients  $\beta$ ,  $\gamma$ , and  $\delta$  are temperature independent, but in many ferroics, including  $\text{CuInP}_2(\text{S}, \text{Se})_6$ ,  $\beta$  or/and  $\gamma$  can change their sign with temperature, pressure, and chemical composition leading to the appearance of tricritical [39], bicritical, and tetracritical points at phase diagrams [40–42]. The values  $\sigma_i$  denote stress tensor diagonal components in the Voigt notations,  $i = 1, 2, 3$ . The values  $Q_{i3}$  and  $Z_{i33}$  denote the linear and nonlinear electrostriction strain tensor components, respectively.  $E_3$  is an electric field, and the last term is the energy of polarization gradient, which strength and anisotropy are defined by the tensor  $g_{33ij}$ .

The values  $T_C$ ,  $\alpha_T$ ,  $\beta$ ,  $\gamma$ ,  $\delta$ ,  $Q_{i3}$  and  $Z_{i33}$  were defined from the fitting of experimentally observed temperature dependence of dielectric permittivity [43–45], spontaneous polarization [46], and lattice constants [24] for hydrostatic and uniaxial pressures (see Fig. 1). The elastic compliances  $s_{ij}$  were estimated from the ultrasound velocity measurements [33,35,47]. These parameters are summarized in Table I. The

TABLE I. LGD parameters for a bulk ferroelectric  $\text{CuInP}_2\text{S}_6$ .

Coefficient	Value
$\varepsilon_b$	9
$\alpha_T$ ( $\text{C}^{-2} \text{ m J/K}$ )	$1.64067 \times 10^7$
$T_C$ (K)	292.67
$\beta$ ( $\text{C}^{-4} \text{ m}^5 \text{ J}$ )	$3.148 \times 10^{12}$
$\gamma$ ( $\text{C}^{-6} \text{ m}^9 \text{ J}$ )	$-1.0776 \times 10^{16}$
$\delta$ ( $\text{C}^{-8} \text{ m}^{13} \text{ J}$ )	$7.6318 \times 10^{18}$
$Q_{i3}$ ( $\text{C}^{-2} \text{ m}^4$ )	$Q_{13} = 1.70136 - 0.00363 T$ , $Q_{23} = 1.13424 - 0.00242 T$ , $Q_{33} = -5.622 + 0.0105 T$
$Z_{i33}$ ( $\text{C}^{-2} \text{ m}^4$ ) <sup>a</sup>	$Z_{133} = -205.965 + 0.8 T$ , $Z_{233} = -121.126 + 0.45 T$ , $Z_{333} = 138.137 - 12 T$
$s_{ij}$ ( $\text{Pa}^{-1}$ ) <sup>b</sup>	$s_{11} = 1.510 \times 10^{-11}$ , $s_{12} = 0.183 \times 10^{-11}$ <sup>b</sup>
$g_{33ij}$ ( $\text{J m}^3/\text{C}^2$ ) <sup>c</sup>	Estimated parameter, which has an order of $10^{-9}$ , e.g., $g \cong (0.5-2.0) \times 10^{-9}$

<sup>a</sup>Note that  $Z_{133}$  and  $Z_{233}$  are negative entire the temperature range, and  $Z_{333}$  becomes negative above 115 K.

<sup>b</sup>Positive  $s_{12}$  means a negative Poisson ratio.

<sup>c</sup>The range of  $g_{33ij}$  agrees with DFT calculations for  $\text{CuInP}_2\text{Se}_6$  [37].

details of their determination are given in Appendix C in Supplemental Material [48].

Note that we estimated, rather than fitted, the value of the polarization gradient coefficients  $g_{33ij}$  from the intrinsic width of the uncharged ferroelectric domain wall observed in CIPS by piezoelectric force microscopy (PFM) [31]. This is an estimation only, because the method cannot separate rigorously the contribution from the tip apex size to the apparent width of the domain wall, as well as the possible broadening of the wall near the surface (see, e.g., Refs. [49,50] for details). Hence, the main problem of  $g$  determination from PFM is that the instrumental resolution function makes a significant contribution to the apparent thickness of the domain walls, so that the intrinsic width is actually less than the observed one, and consequently the  $g$  value obtained from PFM is an upper bound only. Even if the nominal tip size is known, its effective size can be different due to the apex erasure or water meniscus appearance [49]. These effects can decrease the method sensitivity strongly. So, density-functional theory (DFT) calculations giving us the value of the domain walls' surface energy for which the gradient energy can be fitted seem urgent for the case of CIPS.

The jumps on the theoretical curves for the lattice constants variations and spontaneous polarization at about 320 K, shown in Figs. 1(e) and 1(f), respectively, are consequence of the first-order phase transition, since in this case the spontaneous strain and polarization should have a jump in the transition point. The Curie temperature,  $T_C = 292.67$  K, is estimated from the above data and from the jumplike behavior of dielectric permittivity below 320 K at normal pressure [see red points in Fig. 1(b)]. However, the experimental points in Fig. 1(e) do not hint at such jumps, likely due to the smearing of the phase transition by the influence of defects, domain-wall motion, and local electric fields. The smearing appeared significantly smaller for the temperature dependences in Figs. 1(b) and 1(e), where the jumplike behavior is present. Due to the jumplike behavior, we were not able to describe the temperature dependence of polarization and permittivity by simple models, such as 2-4 and 2-4-6 Landau expansion on polarization powers. It appears necessary to include a higher eighth-order degree of polarization in the free energy (1). In this case, the coefficient  $\gamma$  at  $P^6$  turned out to be negative, which indicates the first-order transition. A dashed

zigzaglike curve in Fig. 1(e) is the metastable region, related with the signs  $\beta > 0$  and  $\gamma < 0$ .

Notably, the linear electrostriction coefficients have the signs opposite to the ones, typical of the vast majority of classical perovskite ferroelectrics with  $Q_{11} = Q_{22} = Q_{33} > 0$  and  $Q_{12} = Q_{23} = Q_{13} < 0$  corresponding to a cubic parent phase. The temperature-dependent negative  $Q_{33}$  and positive  $Q_{13} = Q_{13}$  for  $T < 400$  K in CIPS are in complete agreement with the values reported earlier [34]. The unconventional  $Q_{ij}$  signs, which are not forbidden by thermodynamics, can explain the anomalous electromechanical properties of CIPS. Specifically, the existence of the temperature-dependent and negative nonlinear electrostriction  $Z_{i33} < 0$  is the only possibility to fit both the maxima dielectric permittivity and lattice constants temperature dependences. Per Table I,  $Z_{133}$  and  $Z_{233}$  are negative in the temperature range below  $10^3$  K, and  $Z_{333}$  becomes negative above 115 K.

In principle, the nonlinear electrostriction can explain the experimentally observed extremely large elastic nonlinearity in the direction perpendicular to layers [32,33]. Here the nonlinear electrostriction is critically important to describe the polar and dielectric properties of CIPS. The unconventional signs of CIPS electrostriction coefficients explain its negative piezoelectric coefficients, reported earlier [20,21,34].

In most cases, nonlinear electrostriction can be considered as a small correction, and the influence of this effect can be estimated in different ways. For example, it is known that a "linear" electrostriction tensor, which is characterized by  $Q_{ij}$  coefficients, determines two effects: the external pressure dependence of a dielectric permittivity and the value of a spontaneous strain (see Appendix C for details). These facts make it possible to find the coefficients  $Q_{ij}$  from independently obtained experimental data and compare the values obtained by different methods. For some ferroelectrics this procedure has been completed (e.g., for  $\text{BaTiO}_3$  [51]).

In the case of CIPS, there were obvious contradictions between the values of  $Q_{ij}$  extracted from the fitting of dielectric permittivity and spontaneous strain temperature and pressure dependences, respectively. In particular, the signs of several  $Q_{ij}$  coefficients obtained from these two fittings appeared opposite (see Appendix C for details). The only way to resolve the contradiction is to take into account the higher-order electrostriction terms,  $Z_{ij}$ , which do not change

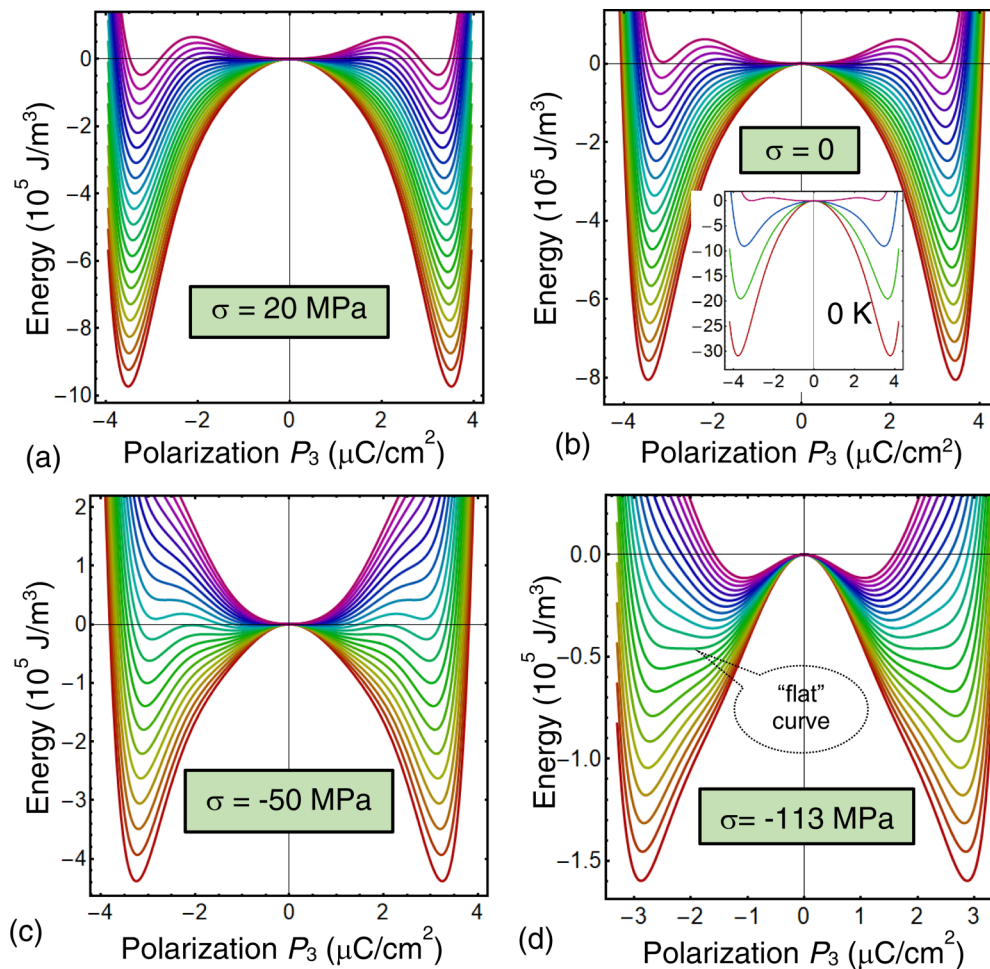


FIG. 2. The dependence of the reconstructed LD energy density (1) on the polarization  $P_3$  calculated for  $E_3 = 0$ , small positive (a), zero (b), small negative (c), and higher negative (d) hydrostatic pressures  $\sigma_1 = \sigma_2 = \sigma_3 = -\sigma$ , respectively. Multiple curves (from red to violet) correspond to different temperatures varying from 210 to 310 K with a step of 5 K for the plots (a), (b), and (c), or from 201.5 to 241.5 K with a step of 2 K for the plot (d). The curves in the inset to the plot (b) corresponds to the temperature  $T = 0, 100, 200,$  and  $300$  K (from the bottom to the top).

the pressure dependence of the permittivity, but affect the spontaneous strain. Exactly the competing contributions of  $Q_{ij}$  and  $Z_{ij}$  resolve the contradiction for CIPS.

We also note that the effects related with nonlinear electrostriction appeared important for other ferroelectrics including BaTiO<sub>3</sub> with negative temperature-dependent coefficient  $\beta$ , that can either change its sign [52] or higher-order expansion coefficients  $\gamma$  and  $\delta$  must be included [53]. Indeed, the characteristic but relatively seldom appreciated feature of such materials is the inclusion of the eighth-order term  $\frac{\delta}{8}P_3^8$  with positive  $\delta$ , which may indicate the existence of other hidden (e.g., antiferroelectric) order parameters [37,38]. Note that the inclusion of  $\frac{\delta}{8}P_3^8$  is mandatory for the stability of thermodynamic potential (1), because  $\gamma < 0$  in the considered case.

The dependence of the reconstructed 2-4-6-8 power LD potential on the polarization  $P_3$  is shown in Fig. 2 for  $E_3 = 0$ . Multiple curves (from red to violet) correspond to different temperatures varying from 210 to 310 K (with a step of 5 K). The plots in Figs. 2(a)–2(d) correspond to positive, zero, small negative, and higher negative hydrostatic pressure  $\sigma_1 = \sigma_2 = \sigma_3 = -\sigma$ , respectively. It is seen from the

plots calculated at  $\sigma = 0$  that the eighth-order potential has two deep and equivalent wells at lower temperatures, which transform into the four nonequivalent wells with the temperature increase [see Fig. 2(b)]. Each two of these four wells correspond to the states with higher and lower spontaneous polarization values, separated by a potential barrier, height and existence of which depend significantly on the temperature. With the temperature increase the deeper well at first lifts up, its depth becomes equivalent with the shallower well, and then eventually disappears, indicating the material transitions to a paraelectric phase. At zero and very small negative pressures the second- and the first-order phase transitions are possible [see Figs. 2(b) and 2(c)], while the high positive pressure makes them of the first order [see Fig. 2(a)]. A high negative pressure makes all these phase transitions of the second order, and the evident case is not shown in the figure.

Application of the intermediate negative pressure significantly complicates the free-energy profile, because the potential wells become shallow and approximately equal, forming an almost “flat” potential curve at a certain value of temperature  $T_0$  and pressure  $\sigma_0$  [see Fig. 2(d)]. The point

$\{T_0, \sigma_0\}$  can be in a special point of coexistence of ferroelectric phases with small and large spontaneous polarization, as well as the paraelectric phase. The special point can be related with the appearance of polycritical points, depending on the number of coexisting phases [39–42]. The behavior of the system in the vicinity of these points is a subject of a separate study; in this work we just point out their existence.

Let us estimate the depth of the potential well  $U_{\min}$  (in units of eV) at the temperatures  $T = 0$  K and  $\sigma = 0$ , within a continuum LGD approach. The approach (in distinction with the first-principles calculations) is applicable for the volumes much higher than the unit cell, because it considers the long-range correlations of the order parameter. Consequently, the minimal volume is a correlation volume, determined by the correlation radius [54]. Actually, according to the Ginzburg-Levanyuk criteria of LGD approach applicability, derived from the Ornstein-Zernike correlator of the order parameter fluctuations, the LGD is applicable if the thermal fluctuations of the order parameter in the correlation volume is small enough in comparison with its average value in the volume [55].

Substitution of the minimal LGD energy density  $g_{\min} \approx -3.1$  MPa [see the bottom curve at 0 K in the inset to Fig. 2(b)], correlation radius  $L_c = \sqrt{\frac{g}{2\alpha_T(T_C-T)}} \approx 0.456$  nm, and corresponding correlation volume  $V_c \cong \frac{4\pi}{3}(3L_c)^3 \approx 10.75$  nm<sup>3</sup> (estimated for  $T = 0$  K and gradient coefficient  $g = 2 \times 10^{-9}$  J m<sup>3</sup>/C<sup>2</sup>) to the expression  $U_{\min} = g_{\min}V_c$ , gives  $U_{\min} = -0.208$  eV. Here the correlation volume  $V_c \cong \frac{4\pi}{3}(3L_c)^3$  corresponds to the conventional exponential polarization correlator  $\langle G \rangle \sim G_0 \exp(-\frac{r}{L_c})$ , giving  $0.05G_0$  for  $r = 3L_c$  [54].

The estimated value  $U_{\min} = -0.208$  eV is surprisingly close to DFT results [see Fig. 1(d) in Ref. [29)]. Since the potential well appears anomalously deep for a small spontaneous polarization  $0.04$  C/m<sup>2</sup>, our result requires a proper verification by the low-temperature measurements of the spontaneous polarization, domain-wall width, and dielectric response. Actually, all experimental data in Fig. 1 are above 100 K, and their fitting by expression (1) in a low-temperature range (0–100) K may be a significant step beyond the limits of the expression applicability.

Taking into account the above restrictions, here we determine all unknown parameters in the LD functional density (1), which is valid for a bulk CIPS in a wide range of temperatures (100–400) K and pressures (0–1) GPa. With these in hand we proceed to calculate the phase diagrams and polar properties of CIPS thin films and nanoparticles.

## B. Phase diagrams and polarization dependences on temperature and stress for a bulk CuInP<sub>2</sub>S<sub>6</sub>

Let us calculate the regions of homogeneous polar ferroelectric (FE) and nonpolar paraelectric (PE) phases existence for a bulk CIPS in dependence on the temperature  $T$  and pressure  $\sigma$  for zero external field ( $E_3 = 0$ ) and without polarization gradient ( $\frac{\partial P_3}{\partial x_i} = 0$ ). To do this we minimize the LD functional and derive the seventh-order algebraic equation for

the determination of spontaneous polarization  $P_3$ ,

$$[\alpha_T(T - T_C) - 2\sigma_i Q_{i3} + (\beta - 4\sigma_i Z_{i33})P_3^2 + \gamma P_3^4 + \delta P_3^6]P_3 = 0, \quad (2)$$

which nonzero solution allows us to analyze the dependence of the spontaneous polarization on  $T$  and  $\sigma$ . Since it appeared that  $\gamma < 0$  for CIPS (see Table I), we cannot neglect the positive term  $\delta P_3^6$  in comparison with the negative term  $\gamma P_3^4$  in Eq. (2). The solution of Eq. (2) is either  $P_3 = 0$  or is given by very cumbersome Cardano formulas. Let us analyze several particular cases.

Since  $\beta < 0$  and the nonlinear electrostriction can be strong, the condition  $\beta - 4\sigma_i Z_{i33} > 0$  cannot be excluded *a priori*. Because of this we need to distinguish the cases  $\beta - 4\sigma_i Z_{i33} > 0$  (realizing a strong nonlinear electrostriction) and  $\beta - 4\sigma_i Z_{i33} < 0$  (corresponding to a weak nonlinear electrostriction).

In the case  $\beta - 4\sigma_i Z_{i33} > 0$  and in the regions where the terms  $\gamma P_3^4 + \delta P_3^6$  in Eq. (2) can be neglected, CIPS undergoes the second-order phase transition between the thermodynamically stable PE phase with  $P_3 = 0$  and FE phase with  $P_3^2 > 0$  under the condition

$$\alpha_T(T - T_C) - 2\sigma_i Q_{i3} = 0. \quad (3a)$$

From Eq. (3a), the temperature of the second-order FE-PE transition is given by the expression  $T_{tr}(\sigma) = T_C - \frac{2}{\alpha_T} \sigma_i Q_{i3}$ . As a matter of fact, the last expression is an equation for the determination of  $T_{cr}(\sigma)$  because  $Z_{i33}$  linearly depends on temperature (see Table I).

In the case  $\beta - 4\sigma_i Z_{i33} < 0$ , the condition (3a) corresponds to the critical temperature of the PE phase absolute instability. In a particular case of zero or very small renormalized coefficient  $[\alpha_T(T - T_C) - 2\sigma_i Q_{i3}]$ , we obtain that the spontaneous polarization is either absent ( $P_3 = 0$ ), or equal to  $(P_3^+)^2 \approx \frac{\sqrt{\gamma^2 - 4(\beta - 4\sigma_i Z_{i33})\delta} - \gamma}{2\delta}$  and  $(P_3^-)^2 \approx \frac{-\sqrt{\gamma^2 - 4(\beta - 4\sigma_i Z_{i33})\delta} - \gamma}{2\delta}$ .

The first special point corresponds to the conditions

$$\alpha_T(T - T_C) - 2\sigma_i Q_{i3} = 0 \quad \text{and} \quad \beta - 4\sigma_i Z_{i33} = 0. \quad (3b)$$

From Eq. (2), the spontaneous polarization in this point is either zero,  $P_3 = 0$ , or nonzero being equal to  $P_3^2 = \frac{\gamma}{\delta}$ . However, this special point is not a tricritical point, because  $\gamma < 0$  and  $\delta > 0$  allow the nonzero polarization. For the application of hydrostatic pressure  $\sigma_1 = \sigma_2 = \sigma_3 = -\sigma$ , the special point can be found from the system of equations  $\beta - 4(Z_{133} + Z_{233} + Z_{333})\sigma_{tcr} = 0$  and  $\alpha_T(T_{tcr} - T_C) - 2\sigma_{cr}(Q_{13} + Q_{23} + Q_{33}) = 0$ .

The boundary of FE phase absolute instability can be found in the following way. The condition of zero second derivative of the potential (1) on  $P_3$  along with Eq. (2) give the equation for polarization values:

$$(\beta - 4\sigma_i Z_{i33})P_3^2 + 2\gamma P_3^4 + 3\delta P_3^6 = 0, \quad (3c)$$

the solutions of which are  $(P_3^+)^2 = \frac{\sqrt{\gamma^2 - 3(\beta - 4\sigma_i Z_{i33})\delta} - \gamma}{3\delta}$  and  $(P_3^-)^2 = \frac{-\sqrt{\gamma^2 - 3(\beta - 4\sigma_i Z_{i33})\delta} - \gamma}{3\delta}$ . These solutions must be substituted back to Eq. (2), which gives us a transcendental equation for the determination of the boundary of FE phase absolute instability.

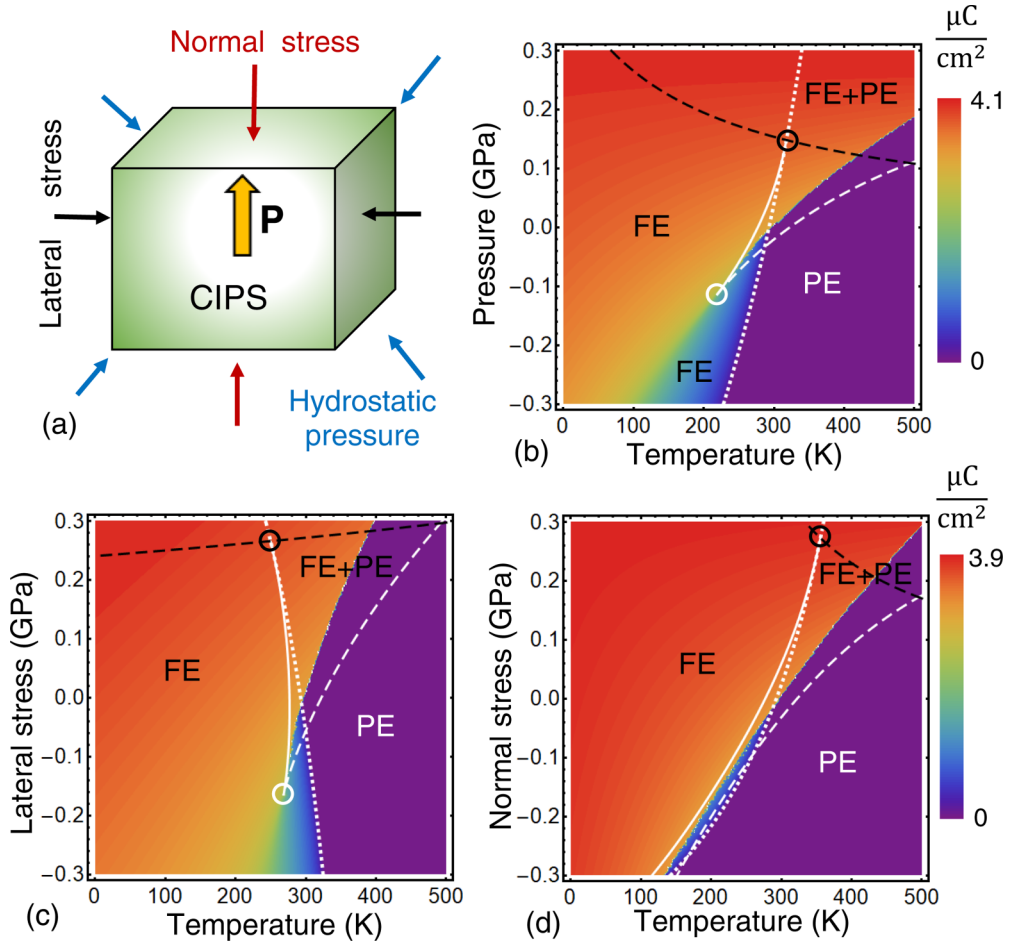


FIG. 3. (a) The bulk of CIPS subjected to an elastic stress or hydrostatic pressure. An orange arrow shows the direction of spontaneous polarization; thin black, blue, and reddish arrows illustrate different ways of applying stress. The dependence of spontaneous polarization  $P_3$  on temperature and hydrostatic pressure (b), lateral biaxial stress (c), and normal uniaxial stress (d). Color scales show the polarization values. White dashed and solid curves are the boundaries of the FE phase absolute instability. White dotted curves correspond to the condition  $\alpha_T(T - T_C) - 2\sigma_i Q_{i3} = 0$ . Black dashed curves show the condition  $\beta - 4\sigma_i Z_{i33} = 0$ . Empty black circles denote the first special point found from the conditions (3b). Empty white circles denote the second special point found from the conditions (3d). CIPS parameters are listed in Table I.

The second special point corresponds to the merging of both solutions of Eq. (3c). In the point  $(P_3^+)^2 = (P_3^-)^2 = \frac{-\gamma}{3\delta}$  and the condition  $\gamma^2 - 3(\beta - 4\sigma_i Z_{i33})\delta = 0$  must be valid. The expression for  $(P_3^\pm)^2$  and the above condition should be substituted to Eq. (2). After elementary transformations this leads to the system of equations for the special point determination:

$$2\sigma_i Q_{i3} = \alpha_T(T - T_C) - \frac{\gamma^3}{27\delta^2} \quad \text{and} \quad \sigma_i Z_{i33} = \frac{1}{4} \left( \beta - \frac{\gamma^2}{3\delta} \right), \quad (3d)$$

where  $Q_{i3}$  and  $Z_{i33}$  linearly depend on  $T$ .

Using expressions (1)–(3) we study the application of hydrostatic pressure  $\sigma_1 = \sigma_2 = \sigma_3 = -\sigma$ , biaxial lateral stress  $\sigma_1 = \sigma_2 = -\sigma$ ,  $\sigma_3 = 0$ , or uniaxial normal stress  $\sigma_1 = \sigma_2 = 0$ ,  $\sigma_3 = -\sigma$  to a bulk CIPS [see Fig. 3(a)]. The dependence of spontaneous polarization  $P_3$  on temperature and hydrostatic pressure, lateral biaxial and normal uniaxial stress are shown in Figs. 3(b)–3(d), respectively, in the form of color maps. Note that the color scale of the spontaneous polarization corresponds to the absolute minimum of the free energy (i.e., to

the deepest potential well), while the polarization value corresponding to the shallower well is not shown. The boundary between the PE and FE phases, as well as their coexistence region, are superimposed on the polarization color maps.

Thus, Figs. 3(b)–3(d) also represent the phase diagrams of a bulk CIPS in coordinates  $\{T, \sigma\}$ . Dotted white curves, satisfying the condition (3a),  $\alpha_T(T - T_C) - 2\sigma_i Q_{i3} = 0$ , correspond either to the second-order PE-FE phase transition curve, or to the boundary of the PE phase absolute instability. Black dashed curves show the condition  $\beta - 4\sigma_i Z_{i33} = 0$ . Empty black circles denote the first special point (3b) corresponding to the intersection of the curves  $\alpha_T(T - T_C) - 2\sigma_i Q_{i3} = 0$  and  $\beta - 4\sigma_i Z_{i33} = 0$ . Note that the color scale of polarization is insensitive to the special point, because numerical solution corresponds to the deepest potential well. The polarization corresponding to the shallower well is sensitive to the special point, but it is not shown in Fig. 3.

The dashed and solid white curves are the boundaries of the FE phase absolute instability. These curves are calculated from the substitution of the two solutions of Eq. (3c) for

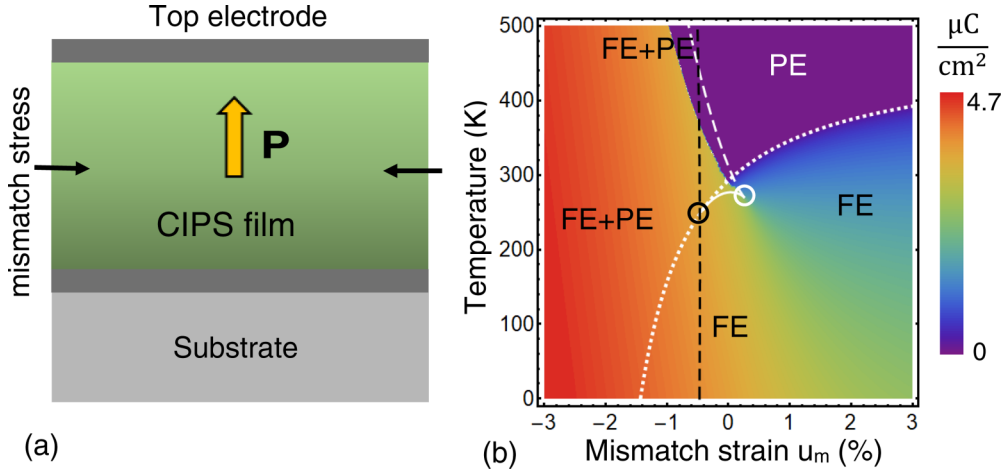


FIG. 4. (a) A CIPS film covered with perfect electrodes and placed on a rigid substrate. An orange arrow shows the direction of the spontaneous polarization; thin black arrows illustrate the strain. (b) The dependence of spontaneous polarization  $P_3$  on temperature and mismatch strain. A color scale shows the polarization values. The dotted, dashed, solid curves, and circles have the same meaning as in Fig. 3. CIPS parameters are listed in Table I.

polarization in Eq. (2), respectively. The curves correspond to the deeper and shallower potential wells (see Fig. 2), and their intersection is the second special point (3d), denoted by the white empty circle in Fig. 3. The coexistence region of the PE and FE phases lies between the dotted and dashed white curves.

The phase diagram, shown in Fig. 3(b), corresponds to the hydrostatic compression (or expansion) of a bulk CIPS. It contains the largest region of FE phase corresponding to compression ( $\sigma > 0$ ), and the smallest region of the phase corresponding to expansion ( $\sigma < 0$ ). The PE-FE boundary is the second-order phase transition at  $\sigma < 0$ , and is the first-order one at  $\sigma > 0$ . The coexistence region denoted as “FE+PE” starts in a critical point located at small negative pressure and expands for zero and positive pressures. The first special point corresponds to  $\sigma \approx 0.15$  GPa and  $T \approx 300$  K; the second special point corresponds to  $\sigma \approx -0.1$  GPa and  $T \approx 210$  K.

The phase diagram, shown in Fig. 3(c), corresponds to the lateral (in-plane) compressive (or tensile) stress of a bulk CIPS. Its structure is similar to the one shown in Fig. 3(b), but the region of FE phase is bigger at  $\sigma < 0$  and smaller at  $\sigma > 0$  than the ones in Fig. 3(b). The first special point corresponds to  $\sigma \approx 0.27$  GPa and  $T \approx 250$  K; the second special point corresponds to  $\sigma \approx -0.16$  GPa and  $T \approx 265$  K.

The phase diagram, shown in Fig. 3(d), corresponds to the normal (out-of-plane) compressive (or tensile) stress of a bulk CIPS. Its structure is different from the ones shown in Figs. 3(a) and 3(b), and the coexistence region FE+PE is much thinner than the ones in Figs. 3(a) and 3(b). The first special point corresponds to  $\sigma \approx 0.3$  GPa and  $T \approx 350$  K, while the second special point is not shown (it corresponds to much higher tensile stress).

The common feature of all diagrams in Fig. 3 is that the FE-PE transition temperature increases and the region of FE phase with a big and small out-of-plane spontaneous polarization  $P_3$  expands for a compressive stress  $\sigma > 0$ . For a tensile stress  $\sigma < 0$  FE-PE transition temperature decreases and the region of FE phase with a small out-of-plane spontaneous

polarization  $P_3$  constricts. The situation is opposite to the one observed for the most uniaxial and multiaxial ferroelectrics, where FE-PE transition temperature decreases and the region of FE phase constricts for  $\sigma > 0$  and expands for  $\sigma < 0$ . The physical origin of the unusual effect is the negative sign of the nonlinear electrostriction coupling,  $Z_{i33} < 0$ , and anomalous signs of the linear electrostriction coupling,  $Q_{33} < 0$ ,  $Q_{23} > 0$  and  $Q_{13} > 0$  (see Table I).

### C. Strain-induced phase transitions in thin $\text{CuInP}_2\text{S}_6$ films

Using the coefficients in thermodynamic potential (1), we can study the strain-induced phase transitions in thin epitaxial  $\text{CuInP}_2\text{S}_6$  films clamped on a rigid substrate [see Fig. 4(a)]. Here we assume that the top surface of the film is mechanically free and the film is placed between conducting electrodes.

Within continuous media approach, the value and orientation of the spontaneous polarization  $P_i$  in thin ferroelectric films can be controlled by their thickness  $h$ , temperature  $T$ , and mismatch strain  $u_m$  originated from the film-substrate lattice constants mismatch [56,57]. The density of the LD free energy, minimization of which allows us to calculate the phase diagram of a strained uniaxial ferroelectric with a homogeneous polarization  $P_3$ , has the form

$$g_L = \frac{\tilde{\alpha}}{2}P_3^2 + \frac{\tilde{\beta}}{4}P_3^4 + \frac{\tilde{\gamma}}{6}P_3^6 + \frac{\tilde{\delta}}{8}P_3^8 - P_3E_3. \quad (4)$$

The coefficients in the expression (4) are renormalized by elastic strains:

$$\begin{aligned} \tilde{\alpha} &= \alpha_T(T - T_C) - 2\frac{Q_{13} + Q_{23}}{s_{11} + s_{12}}u_m + \frac{d_{\text{eff}}}{\epsilon_0\epsilon_f(h + d_{\text{eff}})}, \quad (5a) \\ \tilde{\beta} &= \beta + \frac{(Q_{13} + Q_{23})^2}{s_{11} + s_{12}} + \frac{(Q_{13} - Q_{23})^2}{s_{11} - s_{12}} - 4u_m\frac{Z_{133} + Z_{233}}{s_{11} + s_{12}}, \quad (5b) \end{aligned}$$

$$\tilde{\gamma} = \gamma + 3 \left[ \frac{(Q_{13} + Q_{23})(Z_{133} + Z_{233})}{s_{11} + s_{12}} + \frac{(Q_{13} - Q_{23})(Z_{133} - Z_{233})}{s_{11} - s_{12}} \right], \quad (5c)$$

$$\tilde{\delta} = \delta + 2 \left[ \frac{(Z_{133} + Z_{233})^2}{s_{11} + s_{12}} + \frac{(Z_{133} - Z_{233})^2}{s_{11} - s_{12}} \right]. \quad (5d)$$

Here  $s_{ij}$  are elastic compliances in the Voigt notations;  $u_1 = u_2 = u_m$  are the components of biaxial mismatch strain in Voigt notations. Note that the existence of nonlinear electrostriction leads to the renormalization of the sixth- and eighth-order terms in the energy density (4), at that the term  $\frac{\tilde{\delta}}{8} P_3^8$  appeared not small in comparison with  $\frac{\tilde{\gamma}}{6} P_3^6$  for CIPS. The spontaneous polarization satisfies the seventh-order equation,  $\tilde{\alpha} P_3 + \tilde{\beta} P_3^3 + \tilde{\gamma} P_3^5 + \tilde{\delta} P_3^7 = 0$ .

To derive Eqs. (4) and (5), we substituted the expressions for elastic stresses,  $\sigma_1 = \frac{u_m}{s_{11} + s_{12}} - \frac{s_{11} Q_{13} - s_{12} Q_{23}}{s_{11}^2 - s_{12}^2} P_3^2 - \frac{s_{11} Z_{133} - s_{12} Z_{233}}{s_{11}^2 - s_{12}^2} P_3^4$ ,  $\sigma_2 = \frac{u_m}{s_{11} + s_{12}} - \frac{s_{11} Q_{23} - s_{12} Q_{13}}{s_{11}^2 - s_{12}^2} P_3^2 - \frac{s_{11} Z_{233} - s_{12} Z_{133}}{s_{11}^2 - s_{12}^2} P_3^4$ , and  $\sigma_3 = 0$  into Eq. (1). The derivation details are given in Appendix A. The last term in Eq. (5a) originates from the depolarization field inside the ferroelectric film,  $E_3 = -\frac{P_3}{\epsilon_0 \epsilon_f} \frac{d_{\text{eff}}}{h + d_{\text{eff}}}$  [58], where  $h$  is the film thickness,  $d_{\text{eff}}$  is the thickness of the effective physical gap or dead layer, which may exist at the film surfaces,  $\epsilon_f$  is a relative dielectric permittivity of the film, and  $\epsilon_0$  is a universal dielectric constant. The depolarization effects can be very important in thin films under imperfect screening conditions, e.g., for domain formation [59], but in this section we would like to focus on the strain-induced effects and neglect the depolarization field and polarization gradient effects. This is possible if the effective gap and dead layer are either absent or ultrathin, i.e.,  $d_{\text{eff}} < 0.1$  nm and  $\epsilon_f \gg 1$ , so that the depolarization field becomes very small and the domain formation is not energetically favorable.

The dependence of the spontaneous polarization  $P_3$  on temperature and mismatch strain  $u_m$  is shown in Fig. 4(b). The boundary between the PE and FE phases, as well as their coexistence region, are superimposed on the polarization color maps. The dotted, dashed and solid curves, and circles have the same meaning as in Fig. 3. The diagram contains a relatively small triangularlike region of the PE phase located at temperatures more than 300 K and tensile mismatch strains. The rest of the diagram is filled by the FE phase, which can coexist with the PE phase in the FE+PE region. The PE-FE boundary is the second-order phase transition at tensile strains  $u_m > 0$ , and is the first-order transition at compressive strains  $u_m < 0$ . The FE+PE coexistence region exists for tensile strains only. The first special point corresponds to a small compressive strain  $u_m \approx -0.45\%$  and temperature  $T \approx 250$  K. The second special point is located at small tensile strain  $u_m \approx +0.5\%$  and temperature  $T \approx 265$  K.

The unusual feature of the epitaxial CIPS film diagram is that the high-temperature FE phase with big and small out-of-plane spontaneous polarizations  $P_3^\pm$  exists at a compressive strain  $u_m < 0$ . The phase does not vanish for a tensile strain  $u_m > 0$ ; instead, it expands its area with the increase of  $u_m > 0$ , while the polarization becomes small at  $u_m > 0$

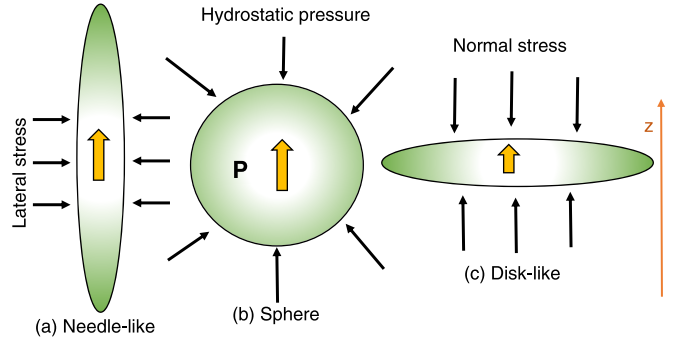


FIG. 5. Considered shapes of CIPS nanoellipsoids. Thick orange arrows show the direction of the spontaneous polarization; thin black arrows illustrate the way of the stress application. A needlelike ellipsoidal nanoparticle stressed in lateral directions with respect to its long axis (a), a hydrostatic compression of the nanosphere (b), and a disklike nanoparticle stressed in the direction normal to its polar axis (c). The spontaneous polarization is directed along the polar axis  $z$  in all three cases.

and eventually undergoes the second-order phase transition at the dotted line. The magnitude of  $P_3$  is big for  $u_m > 0$  and small for  $u_m < 0$ . The situation for  $u_m > 0$  is untypical for the most uniaxial and multiaxial ferroelectric films, where the out-of-plane polarization is absent or very small at  $u_m > 0$ , the region of FE  $c$  phase vanishes or significantly constricts for  $u_m > 0$ , and increases for  $u_m < 0$  [56,57].

The physical origin of the unusual features of the phase diagram of the thin film is similar to the one for the bulk diagrams. It is the negative sum of the high nonlinear electrostriction coupling coefficients,  $Z_{133} + Z_{233}$ , and positive sum of the linear electrostriction coupling coefficients  $Q_{13} + Q_{23}$  (see Table I). The mathematical explanation follows from Eq. (5). Actually, the coefficient  $\tilde{\alpha} = \alpha_T(T - T_C) - 2\frac{Q_{13} + Q_{23}}{s_{11} + s_{12}} u_m$  in Eq. (5a) decreases for  $u_m > 0$ , since  $Q_{13} + Q_{23} > 0$ , while the corresponding coefficient for perovskite films with a cubic parent phase,  $\tilde{\alpha} = \alpha_T(T - T_C) - \frac{4Q_{12}}{s_{11} + s_{12}} u_m$ , increases for  $u_m > 0$ , since  $Q_{12} < 0$  for most perovskites [56]. The coefficient  $\tilde{\beta} = \beta + \frac{(Q_{13} + Q_{23})^2}{s_{11} + s_{12}} + \frac{(Q_{13} - Q_{23})^2}{s_{11} - s_{12}} - 4u_m \frac{Z_{133} + Z_{233}}{s_{11} + s_{12}}$  in Eq. (5b) decreases for  $u_m > 0$ , since  $Z_{133} + Z_{233} < 0$ , while the corresponding coefficient for perovskite films,  $\tilde{\beta} = \beta + \frac{4(Q_{12})^2}{s_{11} + s_{12}}$ , is independent of mismatch strain [56].

The calculated diagram predicts the possibility to increase the FE phase region up to 500 K in the compressed epitaxial CIPS films, and up to 400 K for stretched CIPS films, and the analytical expressions (5) allow us to select the optimal values of  $T$  and  $u_m$  for the phase transitions control. The result can be of particular interest for the strain engineering of CIPS films.

#### D. Stress-induced phase transitions in $\text{CuInP}_2\text{S}_6$ nanoparticles

Using the four-well thermodynamic potential (1), we study the stress-induced phase transitions in CIPS nanoparticles, the shape of which varied from prolate needlelike ellipsoids to oblate disks (see Fig. 5). Note that any type of mechanical action (e.g., hydrostatic pressure, biaxial or uniaxial stress) can be applied to the nanoparticle of arbitrary shape. Leaving the study of a general case for the future, here we consider several

particular cases: a needlelike ellipsoidal nanoparticle stressed (or expanded) in lateral directions with respect to its longer polar axis  $z$  by, e.g., a pore material [Fig. 5(a)], the hydrostatic pressure (or expansion) of the nanosphere [Fig. 5(b)], and a disklike nanoparticle stressed (or expanded) in the direction normal to its short polar axis by, e.g., mechanical clamping [Fig. 5(c)].

We consider the situation when the nanoparticles are placed in a semiconducting medium with a high electric conductivity and a very small effective screening length  $\lambda < 0.1$  nm, which effectively screen their spontaneous polarization in such way to prevent the domain splitting in the particles. That said, we consider single-domain nanoparticles here, leaving the case  $\lambda > 0.1$  nm, when the domain splitting can appear, for future studies.

Taking into account the elastic stress and imperfect screening, the density of the LD energy is

$$g_{LD} = \left( \frac{\alpha^*}{2} - \sigma_i Q_{i3} \right) P_3^2 + \left( \frac{\beta}{4} - \sigma_i Z_{i33} \right) P_3^4 + \frac{\gamma}{6} P_3^6 + \frac{\delta}{8} P_3^8 - P_3 E_3 + g_{33ij} \frac{\partial P_3}{\partial x_i} \frac{\partial P_3}{\partial x_j}, \quad (6a)$$

where

$$\alpha^*(T) = \alpha_T (T - T_C) + \frac{n_d}{\varepsilon_0 [\varepsilon_b n_d + \varepsilon_e (1 - n_d) + n_d (D/\lambda)]}, \quad (6b)$$

Here  $\varepsilon_b$  and  $\varepsilon_e$  are the dielectric permittivity of ferroelectric background [60] and external media, respectively,  $n_d = \frac{1-\xi^2}{\xi^3} (\ln \sqrt{\frac{1+\xi}{1-\xi}} - \xi)$  is the depolarization factor,  $\xi = \sqrt{1 - (R/L)^2}$  is the eccentricity ratio of ellipsoid with a shorter semiaxis  $R$  and longer semiaxis  $L$  [61], and  $D$  is the ellipsoid semiaxis ( $R$  or  $L$ ) in the direction of spontaneous polarization  $P_3$  (see Fig. 5). The derivation of Eq. (6b) is given in Ref. [62]. and Appendix B. In order to focus on the external pressure effect, we neglect the surface tension and polarization gradient effects considered elsewhere [63–65].

It follows from Eq. (6a) that the critical temperature  $T_{cr}$  of the PE phase instability at fixed size  $D$  (or the critical size  $D_{cr}$  at fixed temperature  $T$ ) is determined from the equation  $\frac{1}{2}\alpha^*(T, D) - \sigma_i Q_{i3} = 0$ , where the coefficient  $\alpha^*(T, D)$  is given by Eq. (6b). As it is illustrated below, elastic stresses  $\sigma_i$  can change strongly (in particular increase) the temperature  $T_{cr}$  (or decrease the size  $D_{cr}$ ) of the nanoparticle, and, consequently can enhance their polar properties at operating (e.g., room) temperature and decrease the minimal size of the working element. Thus, an application of elastic stress can be indeed promising for the optimization of CIPS nanoparticles working performances towards superior polar properties. Since it impossible to tell *a priori* what shape of the CIPS nanoparticles is required for different types of fundamental research and/or applications, the influence of stress on their polar properties is illustrated by Fig. 6 for the nanoparticles with various shape.

The dependence of the spontaneous polarization  $P_3$  on temperature and hydrostatic pressure ( $\sigma_1 = \sigma_2 = \sigma_3 = -\sigma$ ), or lateral biaxial stress ( $\sigma_1 = \sigma_2 = -\sigma, \sigma_3 = 0$ ), or

normal uniaxial stress ( $\sigma_1 = \sigma_2 = 0, \sigma_3 = -\sigma$ ) are shown in Figs. 6(b)–6(d) for a nanosphere, a needle, and a nanodisk, respectively. The boundary between the PE and FE phases, as well as their coexistence region, are superimposed on the polarization color maps.

The phase diagram, shown in Fig. 6(b), corresponds to the hydrostatic pressure of a spherical CIPS nanoparticle. It contains the large region of the FE phase with relatively big polarization  $P_3$  corresponding to compression ( $\sigma > 0$ ), and the thin region of the phase with a small  $P_3$  corresponding to expansion ( $\sigma < 0$ ). The PE-FE boundary is the second-order phase transition at  $\sigma < 0$ , and is the first order at  $\sigma > 0$ . The coexistence of FE and PE phases starts in the special point located at  $\sigma \approx -0.20$  GPa and  $T \approx 50$  K, and expands for zero and positive pressures (see the solid and dashed white curves, and white circle). The diagram is similar to the bulk diagram, shown in Fig. 3(a); all the difference consists of the presence of the depolarization field effect, which causes the second term in Eq. (6b) that increases  $\alpha^*(T)$ . As anticipated for any spherical nanoparticles [62–65], the depolarization field effect lowers the temperature for the FE-PE transition, constricts the region of FE phase, and shifts it to the lower temperatures and higher pressures.

The phase diagram, shown in Fig. 6(c), corresponds to the lateral (i.e., perpendicular to the  $z$  axis) compressive (or tensile) stress of a CIPS needlelike nanoparticle. The phase structure is very similar to the bulk diagram shown in Fig. 3(c), the quantitative differences originated from the depolarization effect, which is very small for a needlelike nanoparticle with polarization directed along the long axis of the needle. Actually, the depolarization factor  $n_d \ll 1$  for the case.

The phase diagram, shown in Fig. 6(d), corresponds to the normal (i.e., parallel to the  $z$  axis) compressive (or tensile) stress of a CIPS disklike nanoparticle. Its structure is similar to the bulk diagram shown in Fig. 3(d), but the FE phase and the FE+PE coexistence regions are significantly smaller, thinner, and shifted to lower temperatures in comparison with the corresponding regions in Fig. 3(d). The significant suppression of the FE phase and associated polar properties are related with a strong depolarization effect, since the corresponding depolarization field contribution in Eq. (6b) is not small for nanodisks.

The common feature of the nanoparticle diagrams is that the FE-PE transition temperature and the region of FE phase increase for a compressive stress  $\sigma > 0$ , and decrease for a tensile stress  $\sigma < 0$ . The trend is opposite to the situation observed for many uniaxial and multiaxial perovskite nanoparticles, where FE-PE transition temperature and the region of FE phase increases for  $\sigma < 0$ . The origin of the difference is the negative nonlinear electrostriction coupling  $Z_{i33} < 0$  and “inverted” signs of the linear electrostriction coupling  $Q_{33} < 0, Q_{23} > 0, \text{ and } Q_{13} > 0$  (see Table I). The diagrams, shown in Fig. 6, reveal the strong impact of the elastic stress and shape anisotropy on the polar properties of CIPS nanoparticles with various shapes, required for different types of fundamental research and applications.

Spherical ferroelectric nanoparticles (in reality they are quasispherical, sometimes even more close to cubic) can be easily obtained by, e.g., ball milling [66,67] of a bulk

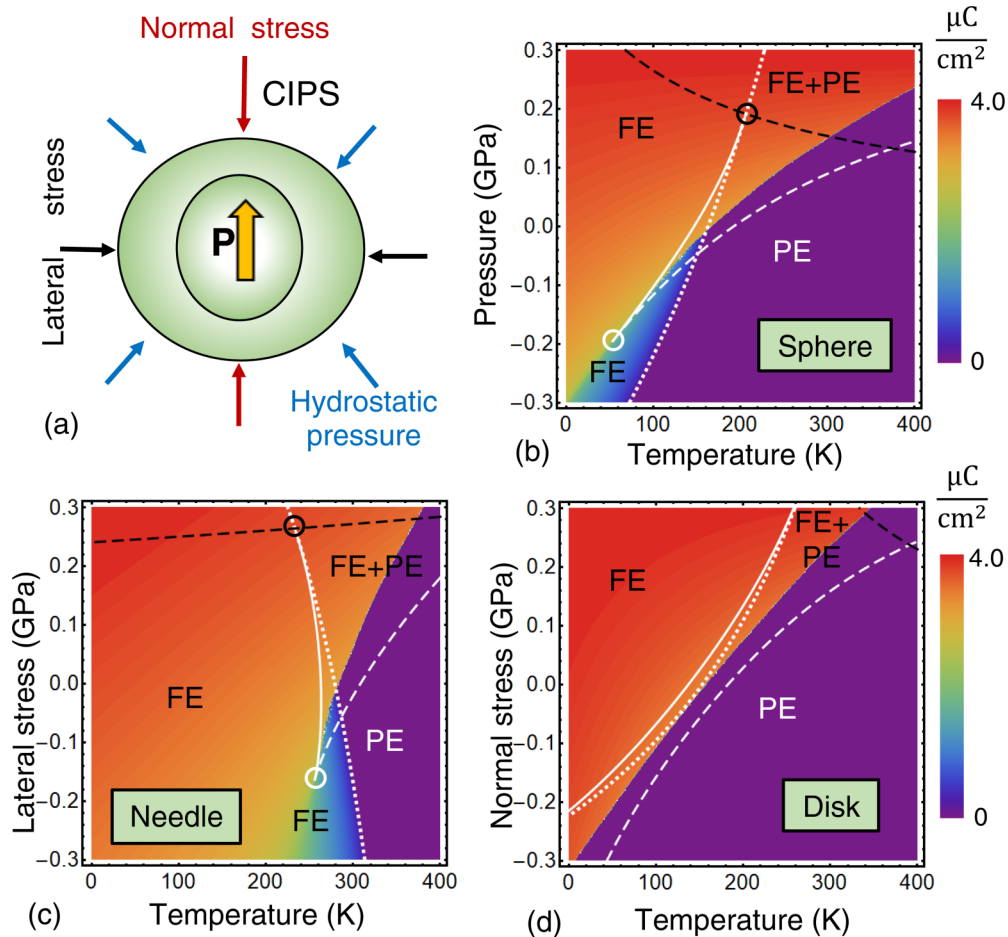


FIG. 6. (a) A CIPS nanoparticle under stress. The dependence of the spontaneous polarization  $P_3$  on temperature and pressure for the stressed CIPS nanosphere with a radius  $R = 20$  nm (b), the needlelike nanoellipsoid with semiaxes  $L = 200$  nm and  $R = 20$  nm (c), and disklike nanoellipsoid with semiaxes  $L = 20$  nm and  $R = 200$  nm (d). The effective screening length  $\lambda = 0.5$  nm,  $\epsilon_e = 2$ . Color scales show the polarization values. The dotted, dashed, solid curves, and circles have the same meaning as in Fig. 3. CIPS parameters are listed in Table I.

material, or advanced chemical vapor deposition (CVD) technology, can be interesting as fillers for various ferroelectric nanocomposites and nanocolloids [68], where the matrix can be polymeric or soft matter [69–71]. These nanocomposites can be used in capacitors, functionalized liquid crystal displays, etc. Our calculations, results of which are illustrated by Fig. 6(b), predict that a hydrostatic pressure can increase strongly the spontaneous polarization and the critical temperature  $T_{cr}$  of ferroelectricity disappearance in a CIPS nanosphere. Also, as it follows from Eq. (6), the pressure can decrease significantly the critical radius  $R_{cr}$  of the nanosphere, which can be useful for the creation of miniaturized CIPS nanospheres with superior polar properties.

It is relatively easy to synthesize (e.g., by self-assembled CVD) CIPS nanowires and long nanorods with rounded ends, which can be modeled theoretically by prolate nanoellipsoids. Either single nanorods or their oriented arrays placed on/in special templates can be interesting and promising for multifunctional applications, such as alternative 3D memories, nanochannels and related logic elements, as well as piezo- or pyro-nanogenerators for energy harvesting [72,73]. For all these applications the prolate shape of a nanoparticle is critically important. Since the spontaneous polarization

is regarded oriented along the nanorod axis, its critical radius of the ferroelectricity disappearance can be essentially smaller than for the nanosphere. This is a relative benefit of a prolate shape. Multiple examples of the interest in ferroelectric nanorods and nanotubes can be found in topical reviews [74,75]. We can imagine that the discovered liquid glass state [76] with additional ferroelectric ordering and other cross-talk effects, are possible in a suspension of the prolate CIPS nanoparticles. Our calculations, results of which are illustrated by Fig. 6(c), predict that a lateral compression can increase significantly the spontaneous polarization and the critical temperature of ferroelectricity disappearance in CIPS needles/nanowires. Also, the compression can decrease the critical radius of the needles, which can be used for the creation of ultrathin polar nanoneedles for versatile multifunctional applications.

The possible interest in CIPS nanodisks is related with the same applications, which are important for nanoflakes and nanoplates of other ferroelectrics [77]. The synthesis of nanoflakes can be much cheaper than the production of thin films, but their polar properties may be worse. Indeed, the typical situation is that the critical thickness corresponding to the ferroelectricity disappearance in a nanodisk with an

out-of-plane polarization is relatively big (e.g., in comparison with a critical radius of a nanowire), but our calculations, results of which are illustrated by Fig. 6(d), predict that normal stresses can decrease the critical size strongly, opening the way for the synthesis of CIPS nanoflakes with conserved polar properties.

### III. CONCLUSION

Using the LD approach and available experimental results we reconstruct the four-well thermodynamic potential for the layered ferroelectric CIPS, which is valid in a wide range of temperatures (100–400) K and applied pressures (0–1) GPa. The simultaneous fitting of independent experimental measurements, such as the temperature dependences of the dielectric permittivity and lattice constants for different applied pressures, unexpectedly reveals the critically important role of a nonlinear electrostriction, which appeared negative and temperature dependent.

With the nonlinear electrostriction included we calculated the phase diagrams and spontaneous polarization of a bulk CIPS in dependence on temperature and pressure. Using the coefficients of the reconstructed thermodynamic potential, we study the strain-induced phase transitions in CIPS thin films, as well as the stress-induced phase transitions in CIPS nanoparticles, the shape of which varies from prolate needles to oblate disks.

The common feature of the bulk and nanoparticle diagrams, shown in Figs. 3 and 6, is that the FE-PE transition temperature increases and the region of FE phase expands for a compressive stress. The feature of the FE phase is the existence of a big and a small out-of-plane spontaneous polarization, corresponding to the deep and shallow wells of the four-well thermodynamic potential. The FE-PE transition temperature decreases, and the region of the FE phase with a small out-of-plane spontaneous polarization constricts for a tensile stress. The situation is opposite to the one observed in the most of uniaxial and multiaxial bulk ferroelectrics.

The unusual feature of the CIPS film diagram, shown in Fig. 4, is that the high-temperature FE phase with a big and small out-of-plane spontaneous polarization, which exists at a compressive strain, does not vanish for a tensile strain, but instead it expands its area, while the polarization becomes small here. The situation for tensile strains is untypical for the most uniaxial and multiaxial ferroelectric films, where out-of-plane polarization is absent or very small for tensile strains [56,57]. The origin of the unusual effects, which we predict for the phase diagrams, is the negative sign of the temperature-dependent nonlinear electrostriction coupling and anomalous signs of the linear electrostriction coupling (see Table I).

To summarize, our calculations predict the strong impact of elastic stress and shape anisotropy on the phase diagrams and polar properties of nanoscale CIPS. We would like to underline that the derived analytical expressions for the renormalized strain- (or stress-) dependent coefficients in the four-well thermodynamic potential allow us to tune the stress/strain range and select the optimal size and shape of the nanoscale CIPS to control its polar properties. Thus, we hope that obtained results can be of particular interest for the stress and strain engineering of nanoscale layered ferroelectrics.

### ACKNOWLEDGMENTS

This material is based upon work (S.V.K, P.M.) supported by the Division of Materials Science and Engineering, Office of Science, Office of Basic Energy Sciences, US Department of Energy, and performed in the Center for Nanophase Materials Sciences, supported by the Division of Scientific User Facilities. A.N.M.'s work is supported by the National Research Foundation of Ukraine (Grant Application 2020.02/0027). Analytical calculations are performed and visualized in the MATHEMATICA 12.2 software [78].

A.N.M. and P.M. generated the research idea and proposed the theoretical model. A.N.M. derived analytical results, interpreted numerical results obtained by E.A.E., and wrote the manuscript draft. S.V.K., Y.M.V., and P.M. worked on the results discussion and manuscript improvement.

- 
- [1] M. Fiebig, Revival of the magnetoelectric effect, *J. Phys. D: Appl. Phys.* **38**, R123 (2005).
  - [2] N. A. Spaldin and M. Fiebig, The renaissance of magnetoelectric multiferroics, *Science* **309**, 391 (2005).
  - [3] A. P. Pyatakov and A. K. Zvezdin, Magnetoelectric and multiferroic media, *Phys. Usp.* **55**, 557 (2012).
  - [4] M. Fiebig, T. Lottermoser, D. Meier, and M. Trassin, The evolution of multiferroics, *Nat. Rev. Mater.* **1**, 16046 (2016).
  - [5] A. P. Pyatakov, Magnetoelectricity goes local: From bulk multiferroic crystals to ferroelectricity localized on magnetic topological textures, *Physica B: Condens. Matter* **542**, 59 (2018).
  - [6] E. Hassanpour, M. C. Weber, Y. Zemp, L. Kuerten, A. Bortis, Y. Tokunaga, Y. Taguchi, Y. Tokura, A. Cano, Th. Lottermoser, and M. Fiebig, *Nat. Commun.* **12**, 2755 (2021).
  - [7] G. Catalan, J. Seidel, R. Ramesh, and J. F. Scott, Domain wall nanoelectronics, *Rev. Mod. Phys.* **84**, 119 (2012).
  - [8] A. A. Bukharaev, A. Zvezdin, A. Pyatakov, and Y. u. Fetisov, Straintronics: A new trend in micro-, nanoelectronics, and material science, *Phys. Usp.* **61**, 1175 (2018).
  - [9] M. D. Glinchuk, A. V. Ragulya, and V. A. Stephanovich, *Nanoferroics* (Springer, Dordrecht, 2013).
  - [10] J. Hlinka, and P. Ondrejovic, Chapter Four-Skyrmions in ferroelectric materials, *Solid State Phys.* **70**, 143 (2019).
  - [11] A. Gruverman, M. Alexe, and D. Meier, Piezoresponse force microscopy and nanoferroic phenomena, *Nat. Commun.* **10**, 1661 (2019).
  - [12] J.-J. Wang, B. Wang, and L.-Q. Chen, Understanding, predicting, and designing ferroelectric domain structures and switching guided by the phase-field method, *Ann. Rev. Mater. Res.* **49**, 127 (2019).
  - [13] D. Zhu, J. Mangeri, R. Wang, and S. Nakhmanson, Size, shape, and orientation dependence of the field-induced behavior in ferroelectric nanoparticles, *J. Appl. Phys.* **125**, 134102 (2019).

- [14] P. Chen, X. Zhong, J. A. Zorn, M. Li, Y. Sun, A. Y. Abid, C. Ren, Y. Li, X. Li, X. Ma, J. Wang, K. Liu, Z. Xu, L. C. Tan, P. Gao, and X. Bai, Atomic imaging of mechanically induced topological transition of ferroelectric vortices, *Nat. Commun.* **11**, 1840 (2020).
- [15] S. A. Pathak and R. Hertel, Three-dimensional chiral magnetization structures in FeGe nanospheres, *Phys. Rev. B* **103**, 104414 (2021).
- [16] S. V. Kalinin, Y. Kim, D. Fong, and A. N. Morozovska, Surface-screening mechanisms in ferroelectric thin films and their effect on polarization dynamics and domain structures, *Rep. Prog. Phys.* **81**, 036502 (2018).
- [17] E. A. Eliseev, Y. M. Fomichov, S. V. Kalinin, Y. M. Vysochanskii, P. Maksymovych, and A. N. Morozovska, Labyrinthine domains in ferroelectric nanoparticles: Manifestation of a gradient-induced morphological phase transition, *Phys. Rev. B* **98**, 054101 (2018).
- [18] A. N. Morozovska, E. A. Eliseev, Y. M. Fomichov, Y. M. Vysochanskii, V. Yu. Reshetnyak, and D. R. Evans, Controlling the domain structure of ferroelectric nanoparticles using tunable shells, *Acta Mater.* **183**, 36 (2020).
- [19] A. N. Morozovska, E. A. Eliseev, R. Hertel, Y. M. Fomichov, V. Tulaidan, V. Yu. Reshetnyak, and D. R. Evans, Electric field control of three-dimensional vortex states in core-shell ferroelectric nanoparticles, *Acta Mater.* **200**, 256 (2020).
- [20] A. Belianinov, Q. He, A. Dziaugys, P. Maksymovych, E. Eliseev, A. Borisevich, A. Morozovska, J. Banys, Y. Vysochanskii, and S. V. Kalinin, CuInP<sub>2</sub>S<sub>6</sub> room temperature layered ferroelectric, *Nano Lett.* **15**, 3808 (2015).
- [21] M. A. Susner, M. Chyasnavichyus, M. A. McGuire, P. Ganesh, and P. Maksymovych, Metal thio- and selenophosphates as multifunctional van der Waals layered materials, *Adv. Mater.* **29**, 1602852 (2017).
- [22] M. Wu and P. Jena, The rise of two-dimensional van der Waals ferroelectrics, *Wiley Interdiscipl. Rev.: Comput. Mol. Sci.* **8**, e1365 (2018).
- [23] F. Liu, L. You, K. L. Seyler, X. Li, P. Yu, J. Lin, X. Wang, J. Zhou, H. Wang, H. He, S. T. Pantelides, W. Zhou, P. Sharma, X. Xu, P. M. Ajayan, J. Wang, and Z. Liu, Room-temperature ferroelectricity in CuInP<sub>2</sub>S<sub>6</sub> ultrathin flakes, *Nat. Commun.* **7**, 12357 (2016).
- [24] M. A. Susner, M. Chyasnavichyus, A. A. Puztzky, Q. He, B. S. Conner, Y. Ren, D. A. Cullen *et al.*, Cation-eutectic transition via sublattice melting in CuInP<sub>2</sub>S<sub>6</sub>/In<sub>4/3</sub>P<sub>2</sub>S<sub>6</sub> van der Waals layered crystals, *ACS Nano*. **11**, 7060 (2017).
- [25] M. Osada and T. Sasaki, The rise of 2D dielectrics/ferroelectrics, *APL Mater.* **7**, 120902 (2019).
- [26] X. Bourdon, V. Maisonneuve, V. B. Cajipe, C. Payen, and J. E. Fischer, Copper sublattice ordering in layered CuMP<sub>2</sub>Se<sub>6</sub> (M = In, Cr), *J. Alloys Compd.* **283**, 122 (1999).
- [27] Y. u. M. Vysochanskii, A. A. Molnar, M. I. Gurzan, V. B. Cajipe, and X. Bourdon, Dielectric measurement study of lamellar CuInP<sub>2</sub>Se<sub>6</sub>: Successive transitions towards a ferroelectric state via an incommensurate phase? *Solid State Commun.* **115**, 13 (2000).
- [28] V. Liubachko, V. Shvalya, A. Oleaga, A. Salazar, A. Kohutych, A. Pogodin, and Y. u. M. Vysochanskii, Anisotropic thermal properties and ferroelectric phase transitions in layered CuInP<sub>2</sub>S<sub>6</sub> and CuInP<sub>2</sub>Se<sub>6</sub> crystals, *J. Phys. Chem. Solids* **111**, 324 (2017).
- [29] J. A. Brehm, S. M. Neumayer, L. Tao, A. O'Hara, M. Chyasnavichyus, M. A. Susner, M. A. McGuire, S. V. Kalinin, S. Jesse, P. Ganesh, S. T. Pantelides, P. Maksymovych, and N. Balke, Tunable quadruple-well ferroelectric van der Waals crystals, *Nat. Mater.* **19**, 43 (2020).
- [30] W. Song, R. Fei, and L. Yang, Off-plane polarization ordering in metal chalcogen diphosphates from bulk to monolayer, *Phys. Rev. B* **96**, 235420 (2017).
- [31] A. Dziaugys, I. Zamaraitė, J. Macutkevicius, D. Jablonskas, S. Miga, J. Dec, Y. u. Vysochanskii, and J. Banys, Non-linear dielectric response of layered CuInP<sub>2</sub>S<sub>6</sub> and Cu<sub>0.9</sub>Ag<sub>0.1</sub>InP<sub>2</sub>S<sub>6</sub> crystals, *Ferroelectrics* **569**, 280 (2020).
- [32] V. Samulionis, J. Banys, and Y. u. Vysochanskii, Linear and nonlinear elastic properties of CuInP<sub>2</sub>S<sub>6</sub> layered crystals under polarization reversal, *Ferroelectrics* **389**, 18 (2009).
- [33] J. Banys, J. Macutkevicius, V. Samulionis, A. Brilingas, and Yu. Vysochanskii, Dielectric and ultrasonic investigation of phase transition in CuInP<sub>2</sub>S<sub>6</sub> crystals, *Phase transitions* **77**, 345 (2004).
- [34] S. M. Neumayer, E. A. Eliseev, M. A. Susner, B. J. Rodriguez, S. Jesse, S. V. Kalinin, M. A. McGuire, A. N. Morozovska, P. Maksymovych, and N. Balke, Giant negative electrostriction and dielectric tunability in a van der Waals layered ferroelectric, *Phys. Rev. Mater.* **3**, 024401 (2019).
- [35] V. Samulionis, J. Banys, and Y. u. Vysochanskii, Piezoelectric and ultrasonic studies of mixed CuInP<sub>2</sub>(S<sub>x</sub>Se<sub>1-x</sub>)<sub>6</sub> layered crystals, *Ferroelectrics* **351**, 88 (2007).
- [36] Y. u. Vysochanskii, R. Yevych, L. Beley, V. Stephanovich, V. Mytrovcij, O. Mykajlo, A. Molnar, and M. Gurzan, Phonon spectra and phase transitions in CuInP<sub>2</sub>(Se<sub>x</sub>S<sub>1-x</sub>)<sub>6</sub> ferroelectrics, *Ferroelectrics* **284**, 161 (2003).
- [37] A. Dziaugys, K. Kelley, J. A. Brehm, L. Tao, A. Puztzky, T. Feng, A. O'Hara, S. Neumayer, M. Chyasnavichyus, E. A. Eliseev, J. Banys, Y. Vysochanskii, F. Ye, B. C. Chakoumakos, M. A. Susner, M. A. McGuire, S. V. Kalinin, P. Ganesh, N. Balke, S. T. Pantelides, A. N. Morozovska, and P. Maksymovych, Piezoelectric domain walls in van der Waals antiferroelectric CuInP<sub>2</sub>Se<sub>6</sub>, *Nat. Commun.* **11**, 3623 (2020).
- [38] A. N. Morozovska, E. A. Eliseev, K. Kelley, Y. u. M. Vysochanskii, S. V. Kalinin, and P. Maksymovych, Phenomenological description of bright domain walls in ferroelectric-antiferroelectric layered chalcogenides, *Phys. Rev. B* **102**, 174108 (2020).
- [39] D. G. Sannikov, Applicability of Landau's theory to phase transitions in the vicinity of a tetracritical point, *Sov. J. Exp. Theor. Phys.* **48**, 863 (1978).
- [40] J. M. Kosterlitz, D. R. Nelson, and M. E. Fisher, Bicritical and tetracritical points in anisotropic antiferromagnetic systems, *Phys. Rev. B* **13**, 412 (1976).
- [41] J. R. Oliver, R. R. Neurgaonkar, and L. E. Cross, A thermodynamic phenomenology for ferroelectric tungsten bronze Sr<sub>0.6</sub>Ba<sub>0.4</sub>Nb<sub>2</sub>O<sub>6</sub> (SBN:60), *J. Appl. Phys.* **64**, 37 (1988).
- [42] R. Folk, Y. u. Holovatch, and G. Moser, Field theory of bicritical and tetracritical points, I. Statics, *Phys. Rev. E* **78**, 041124 (2008).

- [43] P. Guranich, V. Shusta, E. Gerzanich, A. Slivka, I. Kuritsa, and O. Gomonnai, Influence of hydrostatic pressure on the dielectric properties of  $\text{CuInP}_2\text{S}_6$  and  $\text{CuInP}_2\text{Se}_6$  layered crystals, *J. Phys. Conf. Ser.* **79**, 012009 (2007).
- [44] A. V. Shusta, A. G. Slivka, V. M. Kedylich, P. P. Guranich, V. S. Shusta, E. I. Gerzanich, and I. P. Prits, Effect of uniaxial pressure on dielectric properties of  $\text{CuInP}_2\text{S}_6$  crystals Scientific Bulletin of Uzhhorod University, Phys. Ser. **28**, 44 (2010).
- [45] A. Molnar, K. Glukhov, M. Medulych, D. Gal, H. Ban, and Y. u. Vysochanskii, The effect of changes in chemical composition and uniaxial compression on the phase transition of  $\text{CuInP}_2\text{S}_6$  crystals, in *Abstract Book of the FMNT 2020 Online Conference*, Virtual Vilnius, Lithuania (ESCP, 2020), p. 108.
- [46] V. Maisonneuve, V. B. Cajipe, A. Simon, R. Von Der Muhll, and J. Ravez, Ferrielectric ordering in lamellar  $\text{CuInP}_2\text{S}_6$ , *Phys. Rev. B* **56**, 10860 (1997).
- [47] V. Samulionis, J. Banys, Y. u. Vysochanskii, and V. Cajipe, Elastic and electromechanical properties of new ferroelectric-semiconductor materials of  $\text{Sn}_2\text{P}_2\text{S}_6$  family, *Ferroelectrics* **257**, 113 (2001).
- [48] See Supplemental Material at <http://link.aps.org/supplemental/10.1103/PhysRevB.104.054102> for elastic problem solution in thin films, depolarization field inside an ellipsoidal nanoparticle, and high-temperature Landau-Devonshire potential derivation,
- [49] A. N. Morozovska, E. A. Eliseev, G. S. Svechnikov, V. Gopalan, and S. V. Kalinin, Effect of the intrinsic width on the piezoelectric force microscopy of a single ferroelectric domain wall, *J. Appl. Phys.* **103**, 124110 (2008).
- [50] E. A. Eliseev, A. N. Morozovska, S. V. Kalinin, Y. L. Li, J. Shen, M. D. Glinchuk, L. Q. Chen, and V. Gopalan, Surface effect on domain wall width in ferroelectrics, *J. Appl. Phys.* **106**, 084102 (2009).
- [51] F. Jona and G. Shirane, *Ferroelectric Crystals* (Dover Publications, New York, 1993).
- [52] P. Marton, I. Rychetsky, and J. Hlinka, Domain walls of ferroelectric  $\text{BaTiO}_3$  within the Ginzburg-Landau-Devonshire phenomenological model, *Phys. Rev. B* **81**, 144125 (2010).
- [53] A. Kvasov and A. K. Tagantsev, Role of high-order electromechanical coupling terms in thermodynamics of ferroelectric thin films, *Phys. Rev. B* **87**, 184101 (2013).
- [54] B. A. Strukov and A. P. Levanyuk, *Ferroelectric Phenomena in Crystals: Physical Foundations* (Springer, Berlin, 1998).
- [55] A. N. Morozovska and E. A. Eliseev, Surface and finite size effect on fluctuations dynamics in nanoparticles with long-range order, *J. Appl. Phys.* **107**, 044101 (2010).
- [56] N. A. Pertsev, A. G. Zembilgotov, and A. K. Tagantsev, Effect of Mechanical Boundary Conditions on Phase Diagrams of Epitaxial Ferroelectric Thin Films, *Phys. Rev. Lett.* **80**, 1988 (1998).
- [57] C. Ederer and N. A. Spaldin, Effect of Epitaxial Strain on the Spontaneous Polarization of Thin Film Ferroelectrics, *Phys. Rev. Lett.* **95**, 257601 (2005).
- [58] M. V. Strikha, A. I. Kurchak, and A. N. Morozovska, Integer Quantum Hall effect in graphene channel with p-n junction at domain wall in ferroelectric substrate, *J. Appl. Phys.* **125**, 082525 (2019).
- [59] I. Stolichnov, A. K. Tagantsev, E. Colla, N. Setter, and J. S. Cross, Physical model of retention and temperature-dependent polarization reversal in ferroelectric films, *J. Appl. Phys.* **98**, 084106 (2005).
- [60] A. K. Tagantsev and G. Gerra, Interface-induced phenomena in polarization response of ferroelectric thin films, *J. Appl. Phys.* **100**, 051607 (2006).
- [61] L. D. Landau, E. M. Lifshitz, and L. P. Pitaevskii, *Electrodynamics of Continuous Media*, 2nd ed. (Butterworth-Heinemann, Oxford, 1984).
- [62] E. A. Eliseev, A. V. Semchenko, Y. M. Fomichov, M. D. Glinchuk, V. V. Sidsky, V. V. Kolos, Y. u. M. Pleskachevsky, M. V. Silibin, N. V. Morozovsky, and A. N. Morozovska, Surface and finite size effects impact on the phase diagrams, polar and dielectric properties of  $(\text{Sr, Bi})\text{Ta}_2\text{O}_9$  ferroelectric nanoparticles, *J. Appl. Phys.* **119**, 204104 (2016).
- [63] A. N. Morozovska, M. D. Glinchuk, and E. A. Eliseev, Phase transitions induced by confinement of ferroic nanoparticles, *Phys. Rev. B* **76**, 014102 (2007).
- [64] A. N. Morozovska, I. S. Golovina, S. V. Lemishko, A. A. Andriiko, S. A. Khainakov, and E. A. Eliseev, Effect of Vegard strains on the extrinsic size effects in ferroelectric nanoparticles, *Phys. Rev. B* **90**, 214103 (2014).
- [65] A. N. Morozovska, Y. M. Fomichov, P. Maksymovych, Y. M. Vysochanskii, and E. A. Eliseev, Analytical description of domain morphology and phase diagrams of ferroelectric nanoparticles, *Acta Mater.* **160**, 109 (2018).
- [66] I. U. Idehenre, Y. u. A. Barnakov, S. A. Basun, and D. R. Evans, Spectroscopic studies of the effects of mechanochemical synthesis on  $\text{BaTiO}_3$  nanocolloids prepared using high-energy ball-milling, *J. Appl. Phys.* **124**, 165501 (2018).
- [67] Y. u. A. Barnakov, I. U. Idehenre, S. A. Basun, T. A. Tyson, and D. R. Evans, Uncovering the mystery of ferroelectricity in zero dimensional nanoparticles, *R. Soc. Chem., Nanoscale Adv.* **1**, 664 (2019).
- [68] O. Kurochkin, H. Atkuri, O. Buchnev, A. Glushchenko, O. Grabar, R. Karapinar, V. Reshetnyak, J. West, and Y. u. Reznikov, Nano-colloids of  $\text{Sn}_2\text{P}_2\text{S}_6$  in nematic liquid crystal pentyl-cianobiphenile, *Condens. Matter Phys.* **13**, 33701 (2010).
- [69] S. A. Basun, G. Cook, V. Y. Reshetnyak, A. V. Glushchenko, and D. R. Evans, Dipole moment and spontaneous polarization of ferroelectric nanoparticles in a nonpolar fluid suspension, *Phys. Rev. B* **84**, 024105 (2011).
- [70] S. Starzonek, S. J. Rzoska, A. Drozd-Rzoska, K. Czupryński, and S. Kralj, Impact of ferroelectric and superparaelectric nanoparticles on phase transitions and dynamics in nematic liquid crystals, *Phys. Rev. E* **96**, 022705 (2017).
- [71] A. Mertelj, L. Cmok, M. Čopič, G. Cook, and D. R. Evans, Critical behavior of director fluctuations in suspensions of ferroelectric nanoparticles in liquid crystal at nematic to SmA phase transition, *Phys. Rev. E* **85**, 021705 (2012).
- [72] I. I. Naumov, L. Bellaiche, and H. Fu, Unusual phase transitions in ferroelectric nanodisks and nanorods, *Nature (London)* **432**, 737 (2004).
- [73] P. M. Rørvik, T. Grande, and M.-A. Einarsrud, One-dimensional nanostructures of ferroelectric perovskites, *Adv. Mater.* **23**, 4007 (2011).

- [74] J. F. Scott, Applications of modern ferroelectrics, *Science* **315**, 954 (2007).
- [75] J. Varghese, R. W. Whatmore, and J. D. Holmes, Ferroelectric nanoparticles, wires and tubes: Synthesis, characterisation and applications, *J. Mater. Chem. C* **1**, 2618 (2013).
- [76] J. Roller, A. Laganapan, J.-M. Meijer, M. Fuchs, and A. Zumbusch, Observation of liquid glass in suspensions of ellipsoidal colloids, *Proc. Natl Acad. Sci.* **118**, e2018072118 (2021).
- [77] Y. Zhou, D. Wu, Y. Zhu, Y. Cho, Q. He, X. Yang, K. Herrera, Z. Chu, Y. Han, M. C. Downer, H. Peng, and K. Lai, Out-of-plane piezoelectricity and ferroelectricity in layered  $\alpha$ -In<sub>2</sub>Se<sub>3</sub> nanoflakes, *Nano Lett.* **17**, 5508 (2017).
- [78] <https://www.wolfram.com/mathematica>.